Comparison of Rectangular and Dual-Planar Positron Emission Mammography Scanners

Jinyi Qi, *Member, IEEE*, Chaincy Kuo, Ronald H Huesman, *Fellow, IEEE*, Gregory J Klein, *Member, IEEE*, William W Moses, *Senior Member, IEEE*, and Bryan W Reutter, *Member, IEEE*

Abstract— **Breast imaging using dedicated positron emission tomography (PEM) has gained much interest in the medical imaging field. In this paper, we compare the performance between a rectangular geometry and a parallel dual-planar geometry. Both geometries are studied with DOI detectors (detectors capable of measuring the depth of interaction) and non-DOI detectors. We compare the Fisher information matrix, lesion detection, and quantitation of the four systems. The lesion detectability is measured by the signal-to-noise ratio (SNR) of a prewhitening numerical observer for detecting a known hot spot on a uniform background. Results show that the rectangular system with DOI has the highest SNR for the detection task and the lowest bias at any given noise level for the quantitation task. They also show that for small simulated lesions the parallel dual-planar system with DOI detectors outperforms the rectangular system with non-DOI detectors, while the rectangular system with non-DOI detectors can outperform the parallel dual-planar system with DOI detectors for large simulated lesions.**

I. Introduction

Breast imaging using positron emission tomography (PET) has gained much interest in the medical imaging field. Dedicated PET scanners, commonly referred to as positron emission mammography (PEM) cameras, are being developed to improve the cost effectiveness for detecting breast cancers [1-5]. These PEM scanners have special geometries that are different from the conventional circular design of whole body PET scanners. Compared to whole body PET, PEM has much greater sensitivity for detecting breast cancers [3].

A PEM camera (Fig. 1a) is under development at our laboratory that consists of four banks of detector modules (two banks of 3×3 modules left and right and two banks of 3×4 modules top and bottom). As its cross section is rectangular, we refer to this geometry as "rectangular" or "R-PEM." Each detector module consists of an 8×8 array of $3\times3\times30$ mm^3 lutetium oxyorthosilicate (LSO) crystals. The LSO crystals are coupled to a photodiode (PD) array at the front and a photomultiplier tube (PMT) at the back. By measuring the signals from both the PD and the PMT, the depth of interaction (DOI) of the photon can be estimated [4]. For each crystal, the system digitizes DOI information with three bits. Each detector is placed in coincidence with all detectors in the other three banks, giving rise to 172 million possible lines of response (LORs). The maximum field of view (FOV) of the system is $96\times72\times72$ mm^3.

This work was supported by the U.S. Department of Health and Human Services under grant P01 HL25840, by the National Cancer Institute under grant R01 CA 67911, and by the Director, Office of Science, Office of Biological and Environmental Research, Medical Sciences Division of the US Department of Energy under contract DE-AC03-76SF00098.

The authors are with the Center for Functional Imaging, Lawrence Berkeley National Laboratory, Berkeley, CA 94720 USA (telephone: 510-486-4695, e-mail: JQi@lbl.gov).

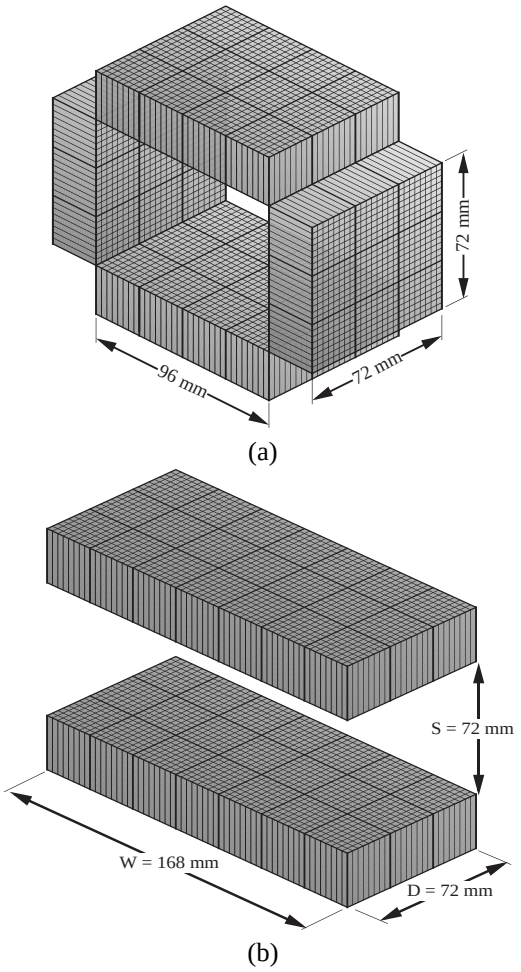

Fig. 1. (a) Rectangular PEM Geometry. (b) Parallel dual-planar PEM.

Another popular design that has been pursued by researchers is a parallel dual-planar geometry (Fig. 1b) [1], [5]. It is similar to using only the top and bottom detector banks in the rectangular PEM scanner. We refer to this geometry as "parallel" or "P-PEM." This design is easier to construct than the rectangular PEM and has greater flexibility in positioning the object into the FOV. However, it suffers from a limited angle of view.

In this paper we explore the imaging performance of these geometries, comparing the R-PEM with the P-PEM for lesion detection and quantitation. Both designs are studied with DOI detectors (detectors that are capable of measuring the depth of interaction) and non-DOI detectors. The P-PEM systems are assumed to be built with the same number of detectors as the R-PEM so that each parallel detector bank has 3×7 detector modules. The width (W) and depth (D) of each detector bank are

168mm and 72mm, respectively. The separation (S) between the two detector banks is 72mm. Each detector is placed in coincidence with all detectors in the opposing bank, giving rise to 115 million LORs for the P-PEM with DOI detectors.

A straightforward method to perform these comparisons is through Monte Carlo simulation. However, such simulations are computationally intensive and the results also depend on the reconstruction algorithm that is used. The latter is a significant problem for novel camera geometries where appropriate algorithms have not yet been developed. We therefore perform these comparisons using the Fisher information matrix, which is computed analytically using the (geometrically determined) forward projection matrix from image space to detector space. This is much faster than running Monte Carlo simulations. Described in more detail in the section below, the Fisher information matrix characterizes how easily a change of one parameter in the source distribution can be identified from the measured data. While there are many ways to parameterize the source distribution, we use a cubic voxel based representation here. To be easily identified, the change at one voxel must make significant contribution to the measurements (as compared with the background noise), and such contribution must not be (strongly) correlated with contributions from other voxels. The Fisher information matrix presents these quantities in a matrix form: the diagonal elements measure the significance of the contribution from each voxel, and the off-diagonal elements measure the correlations. Thus, it can assess the limit of attainable image quality without performing a reconstruction. It can also be used to compute figures of merit for task performance. Here we will use the Fisher information matrix to compute the lesion detectability and the bias/variance trade-off curve.

This paper is organized as follows. In Section II, we describe the Fisher information matrix and how to compute the figures of merit for lesion detection and quantitation. We will put the emphasis on how to use these measures rather than on the mathematical details of the derivation. We present the comparison results of these figures of merit in Section III, where we also study the performance of different P-PEM configurations. In Section IV, we present the conclusion and discuss some limitations of this study.

II. Methods

A. Fisher Information Matrix

The Fisher information matrix is an essential element that determines the limit of image quality of an imaging system. It is defined as [6]

$$\boldsymbol{F} = E\{[\nabla_x L(\boldsymbol{y};\boldsymbol{x})][\nabla_x L(\boldsymbol{y};\boldsymbol{x})]^T\}, \tag{1}$$

or

$$F_{jk} = E\left\{\frac{\partial L(\boldsymbol{y};\boldsymbol{x})}{\partial x_j}\frac{\partial L(\boldsymbol{y};\boldsymbol{x})}{\partial x_k}\right\} \tag{2}$$

$$= E\left\{-\frac{\partial^2 L(\boldsymbol{y};\boldsymbol{x})}{\partial x_j \partial x_k}\right\} \tag{3}$$

where $L(\boldsymbol{y};\boldsymbol{x})$ is the log-likelihood function, $\boldsymbol{y}$ is the observed random variable, $\boldsymbol{x}$ is the unknown image, and $E\{\cdot\}$ denotes expectation with respect to the conditional probability of $\boldsymbol{y}$ given $\boldsymbol{x}$. $\partial L(\boldsymbol{y};\boldsymbol{x})/\partial x_j$ measures the significance of the contribution of a perturbation at voxel j to the data compared with the background noise. The diagonal element F_{jj} measures the magnitude of the contribution, while the off-diagonal element $F_{jk}, j \neq k$ measures the correlation between the contributions from different voxels.

For PET data that can be modeled as a collection of independent Poisson random variables with mean $\bar{\boldsymbol{y}} = \boldsymbol{P}\boldsymbol{x}$, the log-likelihood function is

$$L(\boldsymbol{y};\boldsymbol{x}) = \sum_i (y_i \log \bar{y}_i - \bar{y}_i), \tag{4}$$

and the corresponding Fisher information matrix is

$$\boldsymbol{F} = \boldsymbol{P}^T \mathrm{diag}\left[\frac{1}{\bar{y}_i}\right]\boldsymbol{P}. \tag{5}$$

$\boldsymbol{P}$ is the projection probability matrix with the (i,j)th element being the probability of detecting an event from voxel j at the detector pair i. It includes the solid angle geometric effect, attenuation, and detector response.

One reason that the Fisher information matrix is important is due to its relationship with the variance of the unbiased estimators. Assuming $\boldsymbol{F}$ is nonsingular, the inverse of $\boldsymbol{F}$ is the lower bound of the variance of unbiased estimators, which is often referred to as the Cramer-Rao (CR) lower bound. For PET data with reasonable counts, this bound is very close to the variance of the maximum likelihood (ML) reconstruction, i.e.,

$$\mathrm{var}(\hat{x}_j) \approx [\boldsymbol{F}^{-1}]_{jj} = \mathrm{CR\ bound}, \tag{6}$$

where $\hat{\boldsymbol{x}}$ is the ML reconstructed image.

B. Lesion Detectability

A general approach for studying lesion detectability is to use a receiver operating characteristic (ROC) curve to compare the true positive rate vs. the false positive rate of human observers. The area-under-the-ROC-curve (AUC) is the measure for comparing lesion detectability of different imaging systems. Although human observers are desirable, computer observers are often substituted in ROC studies to reduce cost. Here we use a prewhitening observer, which computes the following test statistic for a given reconstructed image $\hat{\boldsymbol{x}}$ [7]

$$\eta_{\mathrm{PW}}(\hat{\boldsymbol{x}}) = [\bar{\boldsymbol{h}}_1 - \bar{\boldsymbol{h}}_0]^T \Sigma^{-1} \hat{\boldsymbol{x}}, \tag{7}$$

where $\bar{\boldsymbol{h}}_1$ and $\bar{\boldsymbol{h}}_0$ are the mean reconstructions of the image with and without the lesion present, respectively, and Σ is the ensemble covariance matrix of $\hat{\boldsymbol{x}}$. Here we assume that the lesion activity is small enough so that its presence does not change the covariance of $\hat{\boldsymbol{x}}$. From our experience in [13], we believe that the assumption is reasonable when the contribution of the lesion in each LOR is less than a few percent of the projection of the background.

The form in (7) is similar to a matched filter. The use of Σ^{-1} is to decorrelate the noise to improve detection, a procedure called "prewhitening". When noise is normally distributed, the prewhitening observer achieves the optimum performance in detection.

While direct use of (7) would require massive Monte Carlo reconstructions, the advantage of computer observers is that we can theoretically analyze their performance. The detectability of the lesion can be measured by the SNR of $\eta_{\rm PW}(\hat{\boldsymbol{x}})$

$$\begin{aligned} {\rm SNR}^2_{\rm PW} &= \frac{[\eta_{\rm PW}(\bar{\boldsymbol{h}}_1) - \eta_{\rm PW}(\bar{\boldsymbol{h}}_0)]^2}{{\rm var}[\eta_{\rm PW}(\hat{\boldsymbol{x}})]} \\ &= [\bar{\boldsymbol{h}}_1 - \bar{\boldsymbol{h}}_0]^T \Sigma^{-1} [\bar{\boldsymbol{h}}_1 - \bar{\boldsymbol{h}}_0]. \end{aligned} \tag{8}$$

We have shown in [8] that for maximum *a posteriori* (MAP) reconstruction of PET data, the ${\rm SNR}_{\rm PW}$ is

$${\rm SNR}^2_{\rm PW} \approx \boldsymbol{f}_{\rm l}^{\rm T} \boldsymbol{F} \boldsymbol{f}_{\rm l}, \tag{9}$$

where $\boldsymbol{f}_l$ is the lesion profile. Thus, we can compute the lesion detectability using only $\boldsymbol{F}$ and the distribution (in image space) of the lesion. For a small lesion that only occupies voxel j, ${\rm SNR}^2_{\rm PW}$ is proportional to the value of F_{jj}. This means each F_{jj} can be used to measure the detectability of a small lesion at the corresponding location. The larger the F_{jj}, the easier the detection.

Eq. (9) can also be obtained from the asymptotic property of the ML estimator [6]. It is known that the ML estimator is asymptotically efficient and unbiased [9]. Thus the covariance of the ML reconstruction can be approximated by $\boldsymbol{F}^{-1}$ (assuming $\boldsymbol{F}$ is nonsingular) and the difference between the mean reconstructions of the two classes is equal to $\boldsymbol{f}_l$ (unbiased). Combining these results with (8), we can reach (9). The right hand side of (9) is also equal to the SNR of the prewhitening observer when directly applied to the sinogram data.

When $\eta(\hat{\boldsymbol{x}})$ is normally distributed, the SNR is related to the AUC by [10]

$${\rm AUC} = \frac{1}{2}\left[1 + {\rm erf}\left(\frac{\rm SNR}{2}\right)\right], \tag{10}$$

where

$${\rm erf}(x) = \frac{2}{\sqrt{\pi}} \int_0^x \exp(-t^2) dt.$$

Note that the ${\rm SNR}_{\rm PW}$ in (9) is proportional to the contrast of the lesion, but the AUC in (10) is not. As ${\rm SNR}_{\rm PW}$ changes from 0 to $+\infty$, the corresponding AUC monotonically increases from 0.5 to 1 (AUC = 0.98 when SNR = 3). As a result, when the AUC is used to compare lesion detectability, the lesion contrast has to be properly selected so that the AUC is not saturated. There is no such requirement when SNR is used.

C. Quantitation

Quantifying the tumor uptake is another major application of PET imaging. Such quantitation is essential for exploring factors such as tumor growth rate and the efficacy of therapeutic interventions. We estimate the ability of the various camera geometries to measure accurately the tumor activity using the Fisher information matrix.

The uptake of a lesion in a reconstructed image $\hat{\boldsymbol{x}}$ can be measured by

$$\theta = \boldsymbol{f}_l^T \hat{\boldsymbol{x}}.$$

In quantitative studies, we are interested in the bias and the variance of the estimated value θ. These measures can be computed from the Fisher information matrix for small lesions. Here we directly use the results that were derived in [11]:

$${\rm bias}(\theta) \approx \frac{1}{N}\sum_{i=0}^{N-1}\left(\frac{\lambda_i(j)\zeta_i^2}{\lambda_i(j)+\beta}\right) - \boldsymbol{f}_l^T \boldsymbol{f}_l \tag{11}$$

$${\rm var}(\theta) \approx \frac{1}{N}\sum_{i=0}^{N-1}\frac{\lambda_i(j)\zeta_i^2}{(\lambda_i(j)+\beta)^2}, \tag{12}$$

where $\{\lambda_i(j),\ i = 0, \ldots, N-1\}$ is the Fourier transform of the local invariant approximation of the $j{\rm th}$ column of the Fisher information matrix [12], β is the smoothing parameter for the prior function used in [13], and $\{\zeta_i,\ i = 0, \ldots, N-1\}$ is the Fourier transform of the lesion profile $\boldsymbol{f}_l$.

Equations (11) and (12) require that the system response is locally stationary around the lesion and that the noise is relatively low. The first requirement is satisfied for points that are away from the corners with a uniform background. The latter is also satisfied for the activity level simulated in the next section. Comparison of the these approximations with Monte Carlo simulated results can be found in [13], [11].

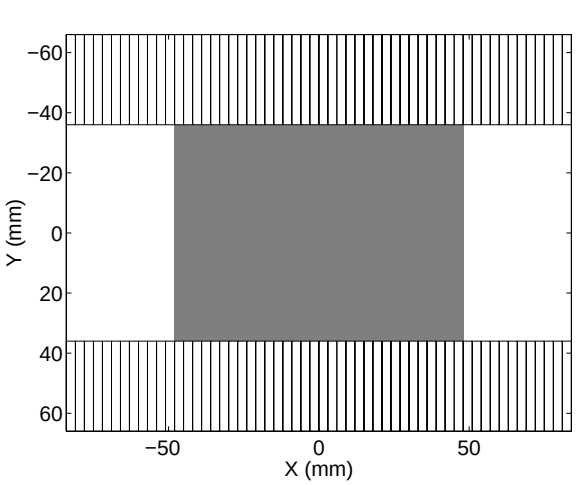

Fig. 2. The front view of the uniform flood source phantom in the P-PEM geometry. The phantom is placed at the center of the FOV with two detector banks at top and bottom.

III. Simulation Results

We simulated the background using a $96\times72\times72$ mm^3 uniform flood phantom, which filled the whole FOV of the R-PEM scanners. In P-PEM simulations, the phantom was placed at the center of the FOV as shown in Fig. 2. The detection probability matrix $\boldsymbol{P}$ was calculated using the method described in [14] assuming an attenuation length of 100mm inside the FOV and an attenuation length of 10mm inside detector crystals. Neither scatters nor randoms were simulated.

The background activity was estimated by assuming a subject weighing 70kg, an injection of 1 mCi of F-18-labeled deoxyglucose, and an imaging time of 1 minute. This activity density resulted in about 2 million detected events for R-PEM scanners, and about 1 million detected events for P-PEM scanners. Previous work has shown that this gives noise similar to a 10 minute scan (with the same injected activity) that includes scatters [14].

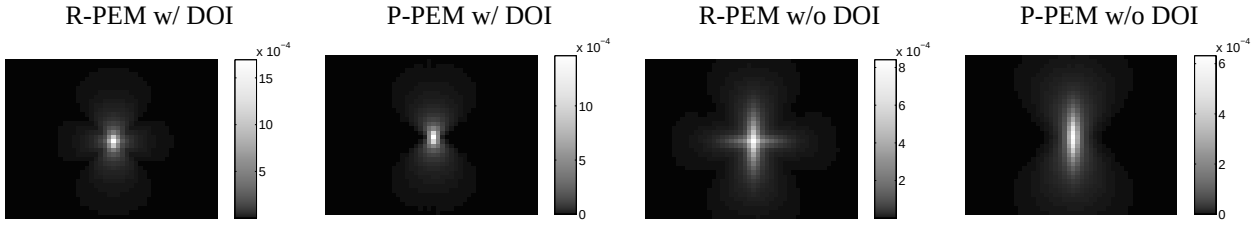

Fig. 3. Comparison of front view slices of Fisher information images of four PEM systems for the center voxel. The maximum values are, from left to right, 16.9×10^{-4}, 14.8×10^{-4}, 8.4×10^{-4}, and 6.3×10^{-4}.

There was no limit on the maximum acceptance angle for P-PEM scanners, since we would use an iterative algorithm to reconstruct the data.

A. Comparison of Fisher Information

Fig. 3 shows the front view slices of the Fisher information images of the center voxel for the four systems. Each image is the front view slice through the center of the 3D volume representations of the column vector $\boldsymbol{F}_{*j}$, where j is the index of the center voxel. $\boldsymbol{F}_{*j}$ was computed using (5) as follows: first compute the noise-free projection of a point source located at voxel j, then weight the point source projection by the inverse of the variance of the background projection, and finally backproject the weighted point source projection.

The images in Fig. 3 can be thought of as showing the correlation between the voxel containing a source (in this case the center voxel) and the rest of the voxels. An ideal system would have a very large value for the voxel containing the source – this indicates that the system is sensitive to small changes in this voxel. This value is also proportional to the SNR^2 of detecting a small lesion in this voxel. An ideal system would also have zero values for all voxels that do not contain the source, indicating that there is no correlation at all and the system can easily distinguish a source placed in one voxel from a source placed in another voxel. In practice, correlations do exist and the off-diagonal elements ($F_{jk}, j \neq k$) are non-zero. Their effect depends on the specific application of the system. For some tasks these non-zero values can even be helpful (see [6] for more discussions).

Clearly the R-PEM with DOI has the largest F_{jj}. The F_{jj} of the P-PEM with DOI is 86% of that of the rectangular R-PEM. For the systems without DOI, the F_{jj} of the R-PEM drops to 50%, and the P-PEM drops to 37%. The Fisher information images for the non-DOI systems are elongated in the vertical and horizontal (R-PEM only) directions because the crystal length is 30 mm. Such elongation can be reduced by using shorter detector crystals, however, this would be at the cost of reducing the overall sensitivity.

To compare the system properties when the source is placed in other locations, we compute F_{jj} of other voxels in the FOV, and then compute the ratio of F_{jj} between the R-PEM and the P-PEM (both with DOI). Fig. 4 shows the three orthogonal views through the center of the ratio image (the value of the P-PEM divided by that of the R-PEM). The results show that the ratio is the largest (close to 90%) near the center of the transaxial FOV, and it is nearly constant in the axial direction. As the location moves away from the transaxial center, the ratio becomes

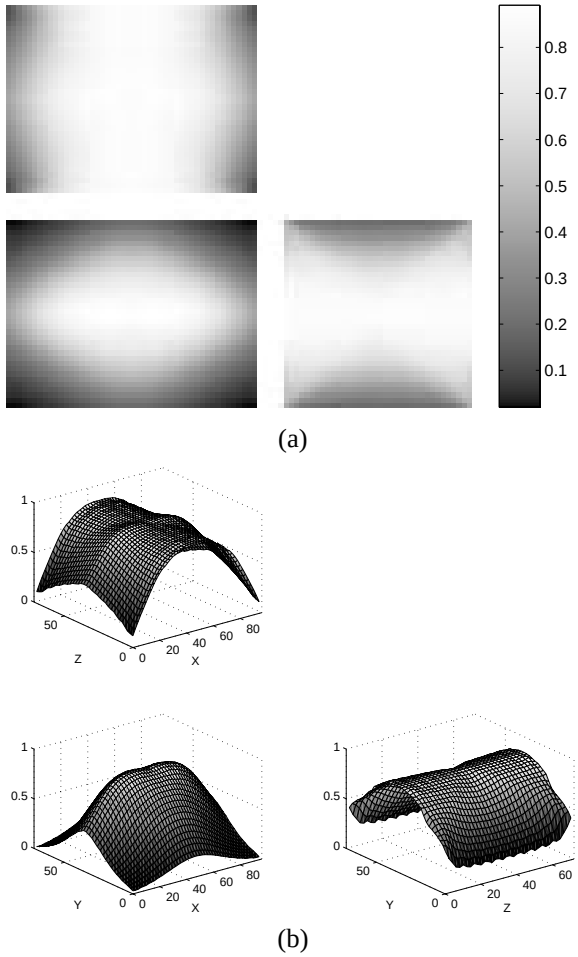

Fig. 4. The ratio of F_{jj} between the P-PEM and the R-PEM both with DOI. (a) Three orthogonal views through the center of the ratio image: top view (top), front view (lower left), and side view (lower right). (b) The corresponding surface plots.

smaller. This indicates that the advantages of the R-PEM over the P-PEM are likely to be less significant for the center region in the transaxial FOV, and be more significant at off-center locations. In the following comparison we will focus on the center voxel.

B. Comparison of Lesion Detectability

Fig. 5 shows the comparison of the SNRs for lesion detection as functions of the lesion size for all four systems. The simulated lesions are spherical with different diameters and are located at the center of the FOV. The contrast of the lesion ([lesion activ-

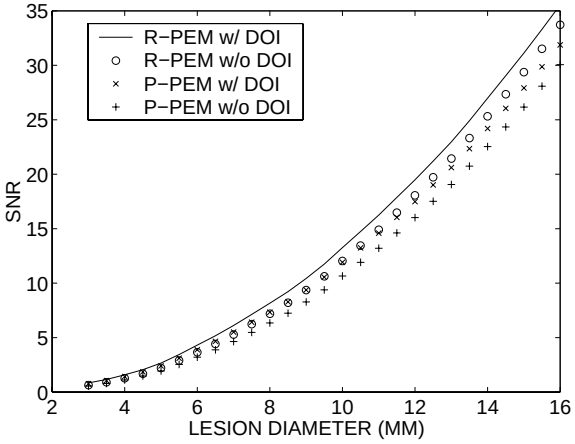

(a)

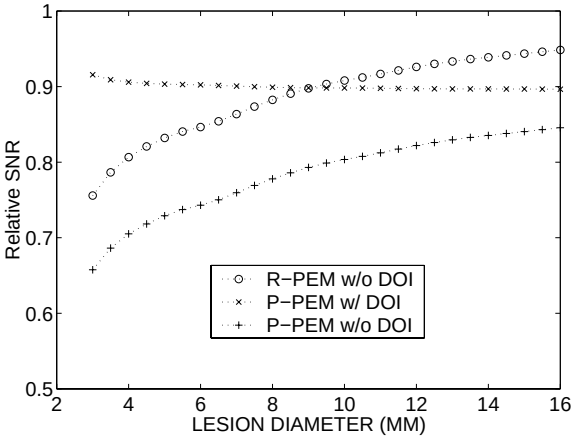

(b)

Fig. 5. (a) Plots of SNR vs. lesion size for all four systems. (b) The relative SNR of the other three systems when normalized by the SNR of the R-PEM with DOI.

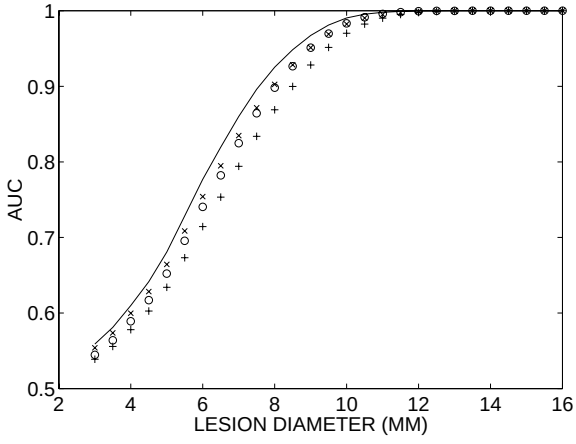

(a)

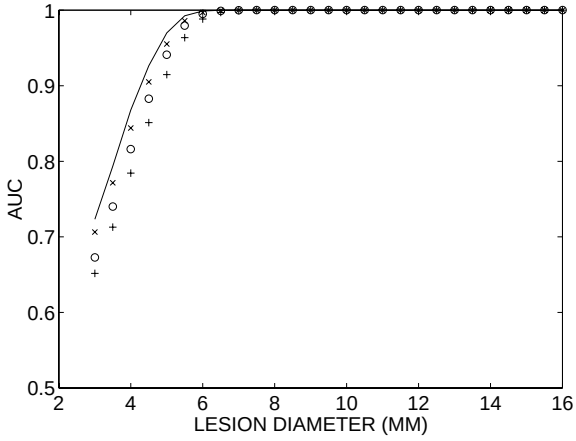

(b)

Fig. 6. Plots of AUC vs. lesion size for all four systems. (a) Lesion with true contrast of 1/4; (b) lesion with true contrast of 1. The symbols represent rectangular with DOI (solid line), planar with DOI ('×'), rectangular without DOI ('o'), and planar without DOI ('+').

ity - background]/background) was one. Fig. 5(a) shows that all SNRs increase as the lesion size increases. The relative performance of the four systems, normalized by the SNR of the R-PEM with DOI, is shown in Fig. 5(b). The SNR of the P-PEM with DOI is about 90% of that of the R-PEM with DOI. For small lesions, the order of the SNRs of the four systems is R-PEM with DOI $>$ P-PEM with DOI $>$ R-PEM w/o DOI $>$ P-PEM w/o DOI. As lesion size increases, the relative performance of the systems without DOI increases. For lesions with diameter larger than 9mm, the SNR of the R-PEM w/o DOI is greater than the SNR of the P-PEM with DOI. We know from (9) that SNR is proportional to the lesion contrast, so when the contrast increases (or decreases), the curves in Fig. 5(a) will move up (or down) accordingly, but the curves in Fig. 5(b) will stay the same.

From Fig. 5, we can compute the AUC using (10). Fig. 6 shows the plots of the AUC as a function of the lesion size for all four systems. In Fig. 6(a), the true contrast of the lesion is 1/4 and in Fig. 6(b), the contrast is one. As expected, the AUC increases as the size of lesion increases. In addition, for the lesion with contrast of 1/4 (Fig. 6(a)), significant differences among the AUCs of the four systems can be seen when lesion size is between 6mm and 9mm, whereas for the lesion with contrast of one (Fig. 6(b)), such differences can be seen when lesion size is between 3mm and 5mm.

Fig. 7 shows the plots of the AUC as a function of the lesion contrast for all four systems. The diameters of the simulated spherical lesions are 3mm for Fig. 7(a) and 6mm for Fig. 7(b). Clearly, the AUC increases as the contrast increases. Similar to Fig. 6, it shows that for the 3mm lesion (Fig. 7(a)), significant differences among the AUCs of the four systems can be seen when the lesion contrast is around 3, whereas for the 6mm lesion (Fig. 7(b)), the differences are significant when the contrast is around 0.5.

Both Fig. 6 and Fig. 7 show that the geometry and DOI information only have significant impact on detection of lesions in a certain range (size and contrast combination) when the AUC is used to measure the lesion detectability. For small, low contrast lesions that are extremely hard to detect, or large, high contrast lesions that are very easy to identify, all the systems may perform the same in terms of the AUC measure.

In all Figures, R-PEM with DOI has the best performance and the P-PEM without DOI has the worst performance. For small lesions the P-PEM with DOI outperforms the R-PEM without DOI, while the reverse can be true for large lesions. This can be

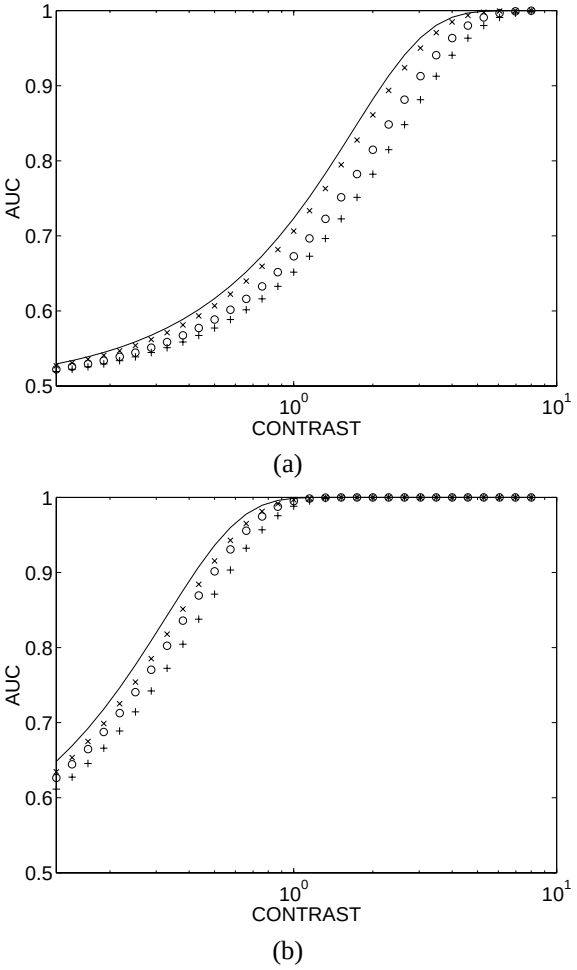

Fig. 7. Plots of AUC vs. contrast of the lesion for all four systems. (a) A 3mm diameter lesion; (b) a 6mm diameter lesion. The symbols represent rectangular with DOI (solid line), planar with DOI (‘×’), rectangular without DOI (‘o’), and planar without DOI (‘+’).

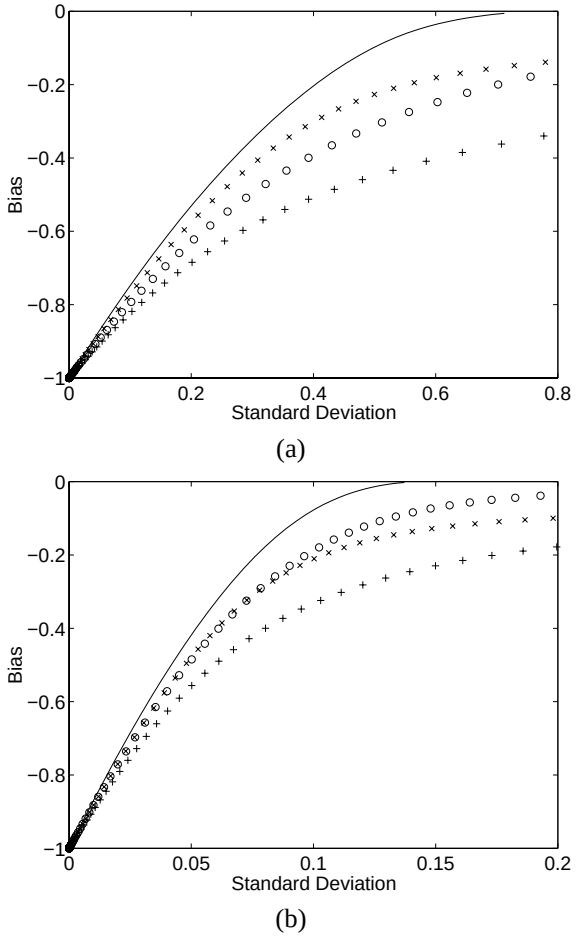

Fig. 8. Plots of bias vs. standard deviation of quantitation of mean activity in different lesions for all four systems: (a) a 6mm diameter lesion; (b) a 10mm diameter lesion. The symbols represent rectangular with DOI (solid line), planar with DOI (‘×’), rectangular without DOI (‘o’), and planar without DOI (‘+’). The true contrast of the lesion is one.

understood by considering the qualitative strengths and weaknesses of the two designs. P-PEM with DOI has better spatial resolution but lower sensitivity than R-PEM without DOI. For small lesions, spatial resolution is probably more important than sensitivity, so the P-PEM with DOI should outperform the R-PEM without DOI. For large lesions, spatial resolution is less important, and so the design with higher sensitivity (the R-PEM without DOI) should perform better.

C. Quantitation

For each system, we calculated the bias and variance of the lesion quantitation using (11) and (12) with the corresponding Fisher information matrix. We studied two spherical lesions: one 6mm diameter and one 10mm diameter. For an easy comparison between different lesions, we normalized the bias and the standard deviation by the energy of the lesion, $\boldsymbol{f}_l^T \boldsymbol{f}_l$. Fig. 8 shows the plots of the normalized bias vs. standard deviation for all four systems. The different points on each curve were obtained by varying the smoothing parameter β. Under all situations, the R-PEM with DOI performs the best (the least bias at any standard deviation) and the P-PEM w/o DOI performs the worst. As was the case for lesion detection, for the small lesion the P-PEM with DOI performs better than the R-PEM w/o DOI, while for the large lesion the R-PEM w/o DOI can perform better than P-PEM with DOI.

D. Performance of Different P-PEM Configurations

It has been shown that in some cases, P-PEM performance improves with compression [15]. In this section we study the performance of the P-PEM system with different detector separation (S) and detector width (W) (see Fig. 1b) using the Fisher information matrix. We simulate different widths, as well as allowing compression (i.e., reducing the separation while simultaneously “deforming” the phantom). The results are compared with the P-PEM configuration that we studied above (S=72mm, W=168mm).

D.1 Vertical Compression (Detector Bank Separation)

In this section we study the effect of applying compression on the breast being imaged. The vertical compression generally reduces the separation between the two detector banks. This will increase the solid angle coverage for the center of the FOV. However, for locations near the boundary the results may vary. In this study we assume the breast has a fixed volume in the

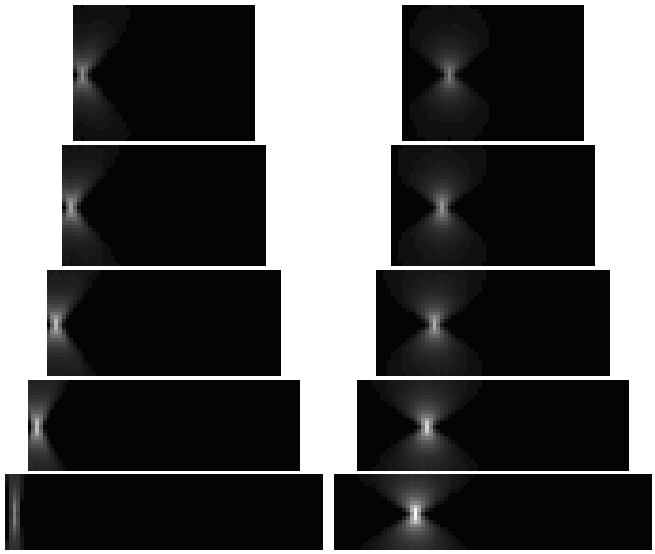

(a) (b)

Fig. 9. Front view slices of the Fisher information images for two points of interest in a P-PEM system with different compression: (a) a point near the boundary; (b) a point in the bulk. The separation between the two detector banks are, from top to bottom, 72mm, 64mm, 56mm, 48mm, and 40mm, respectively. All the images are in the same gray scale.

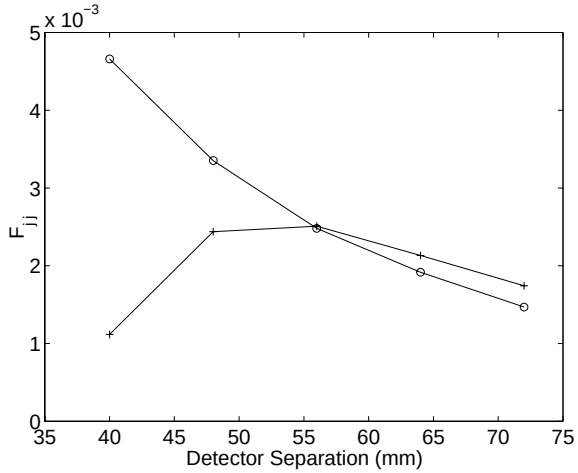

Fig. 10. Plots of the Fisher information (maximum values of each image shown in Fig. 9) of the two points of interest as a function of distance between of the two detector banks. The '+'s denote the boundary point and the 'o's denote the point in the bulk.

(a) (b) (c)

Fig. 11. Front view center slice of the F_{jj} image of P-PEM systems: (a) detector horizontal width = 96mm; (b) detector horizontal width = 168mm; (c) detector horizontal width = 216mm. The images are in the same gray scale and the intensities of the corner pixels in (b) and (c) are truncated to show the details in the bulk of the images. Lighter color indicates higher value.

FOV, i.e., when it is compressed, the width increases proportionally (this may not be exact in real situations). We selected two points of interest: one near the boundary, and one in the bulk. For the boundary point, we keep it at a fixed distance (5mm) from the boundary of the object. For the one in the bulk, we keep it midway between the center and the boundary of the object. Fig. 9 shows the front view slices of the Fisher information images for the two points of interest at various compression conditions. Fig. 10 shows the plot of F_{jj} as a function of detector bank separation for the two points. For the point near the boundary, F_{jj} increases with a small amount of compression, but drops as the compression increases beyond a certain point. This is because with large compression the point gets near the edge of the detector banks, where the solid angle is very limited. For the point in the bulk, F_{jj} monotonically increases as the vertical separation between the detector banks decreases. The results show that moderate compression is helpful for lesion detection (the SNR^2 increases by almost a factor of 3) as long as the lesion is not close to the boundary of the FOV of the scanner.

D.2 Width of the Detector Banks

For the P-PEM design, it is helpful to use extra detector modules so that the FOV of the scanner is larger than the object being imaged. This greatly improves the uniformity of the sensitivity in the horizontal direction although it requires additional detector modules. Here we use F_{jj} to study the performance of P-PEM systems with detectors of different horizontal width. We assume the object being imaged is a $96\times72\times72$ mm^3 volume placed in the center of the FOV of the scanner.

Fig. 11(a) shows the center front view slice of the F_{jj}'s for the P-PEM system with the horizontal width of the detector equal to 96mm, which exactly covers the object (lighter color indicates higher value of F_{jj}, which in turn indicates higher SNR). F_{jj} drops to zero at the horizontal boundary of the object because of the limited angle. Fig. 11(b) shows the F_{jj}'s for the P-PEM system with the horizontal width of the detector equal to 168mm. This is the P-PEM system that we characterized in previous sections. Clearly, by using a few extra detectors in the horizontal direction, the sensitivities at the boundary are much improved. The F_{jj} image is almost uniform except for the corners. Fig. 11(c) shows the F_{jj}'s for the P-PEM system with the horizontal width of the detector equal to 216mm. The improvement over Fig. 11(b) is marginal. Fig. 12 compares the horizontal profiles through the center of the images shown in Fig. 11 (and three more cases). It shows that when the horizontal width is increased from 96mm, the sensitivity of the system is greatly improved. However, as the width exceeds 168mm, only the sensitivities at the boundaries are marginally increased. The 168mm design has a good balance between the overall sensitivity and detector cost, and thus appears to be the "optimal" width for this size phantom.

IV. Conclusions and Discussion

We have presented comparisons between the rectangular and planar PEM scanners for lesion detection and quantitation. In all cases, the rectangular system with DOI performs the best (highest signal-to-noise ratio for lesion detection and the lowest bias at any given noise level for quantitation), while the parallel dual-

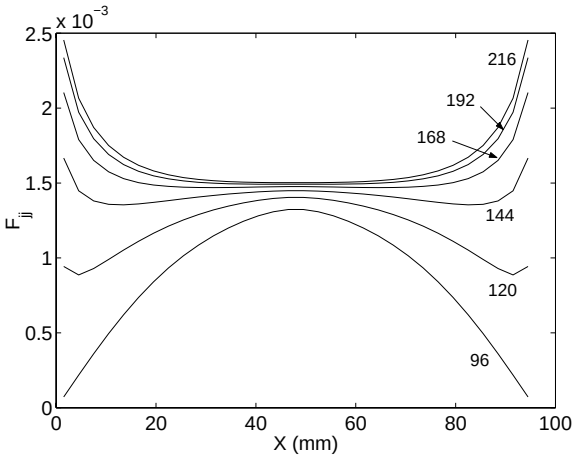

Fig. 12. Horizontal profiles through the center of the front view center slice of the F_{jj} for P-PEM systems with different detector widths. The horizontal widths of the detector banks for each curve are, from the top to bottom, 216mm, 192mm, 168mm, 144mm, 120mm, and 96mm, respectively.

planar system without DOI performs the worst. It also shows that for small lesions the parallel dual-planar system with DOI detectors outperforms the rectangular system with non-DOI detectors, while the rectangular system with non-DOI detectors can outperform the parallel dual-planar system with DOI detectors for large lesions.

We have also studied the performance of different dual-planar PEM configurations. We found that (1) detector bank size should be reasonably ($\sim$50%) larger than the object of interest to achieve uniform sensitivity and (2) moderate compression is helpful for lesion detection as long as the lesion is not close to the boundary of the FOV of the scanner. One flexibility of dual-planar PEM that was not explored in the paper is the positioning of the object. This may be important for detecting a lesion that is near the chest wall, since such lesion would lie near the axial edge of the FOV of all PEM systems in the standard setup, where the sensitivity is very low. By moving the two detector banks, it is possible to place such lesions close to the center of the FOV for dual-planar PEM systems.

The results presented in this paper are all based on the assumption that all four systems use an iterative statistical reconstruction algorithm with accurate modeling of the detector penetration effect, and that the algorithm is iterated until convergence. Therefore, these results do not necessarily apply to reconstructions obtained using filtered backprojection, iterative algorithms with a simple line-integral model, or ordered-subset algorithms with stopping rules. In addition, the lesion detection task used here is a "signal-known-exactly, background-known exactly" task. Some results may change if randomness in the lesion and the background is included, which is an ongoing research topic.

ACKNOWLEDGMENTS

The authors would like to thank the anonymous reviewers for their valuable comments.

This work was supported by the U.S. Department of Health and Human Services under grant P01 HL25840, by the National Cancer Institute under grant R01 CA 67911, and by the Director, Office of Science, Office of Biological and Environmental Research, Medical Sciences Division of the US Department of Energy under contract DE-AC03-76SF00098.

REFERENCES

[1] C. Thompson, K. Murthy, Y. Picard, I. Weinberg, and R. Mako, "Positron emission mammography (PEM): A promising technique for detecting breast cancer," *IEEE Transactions on Nuclear Science*, vol. 42, pp. 1012–1017, 1995.

[2] I. Weinberg, S. Majewski, A. Weisenberger, A. Markowitz, L. Aloj, L. Majewski, D. Danforth, J. Mulshine, K. Cowan, J. Zujewski, C. Chow, E. Jones, V. Chang, W. Berg, and J. Frank, "Preliminary results for positron emission mammography - real-time functional breast imaging in a conventional mammography gantry," *European Journal Of Nuclear Medicine*, vol. 23, pp. 804–806, 1996.

[3] R. Freifelder and J. S. Karp, "Dedicated PET scanners for breast cancer," *Physics in Medicine and Biology*, vol. 42, pp. 2463–2480, 1997.

[4] W. W. Moses, S. E. Derenzo, C. L. Melcher, and R. A. Manente, "A room temperature LSO/PIN photodiode PET detector module that measures depth of interaction," *IEEE Transactions on Nuclear Science*, vol. 42, pp. 1085–1089, 1995.

[5] N. Doshi, Y. Shao, R. Silverman, and S. Cherry, "Design and evaluation of a LSO PET detector for breast cancer imaging," *Medical Physics*, vol. 27, pp. 1535–1543, 2000.

[6] H. H. Barrett, J. L. Denny, R. F. Wagner, and K. J. Myers, "Objective assessment of image quality. II. Fisher information, Fourier crosstalk, and figures of merit for task performance," *Journal of Optical Society of America A*, vol. 12, pp. 834–852, 1995.

[7] H. H. Barrett, "Objective assessment of image quality: Effects of quantum noise and object variability," *Journal of the Optical Society of America A*, vol. 7, pp. 1266–1278, 1990.

[8] J. Qi and R. H. Huesman, "Theoretical study of lesion detectability of MAP reconstruction using computer observers," *IEEE Transactions on Medical Imaging*, vol. 20, pp. 815–822, 2001.

[9] H. L. Van Trees, *Detection, Estimation, and Modulation Theory, Part I*, John Wiley&Sons, 1968.

[10] H. H. Barrett, G. K. Abbey, and E. Clarkson, "Objective assessment of image quality. III. ROC matrics, ideal observers, and likelihood-generating functions," *Journal of Optical Society of America A*, vol. 15, pp. 1520–1525, 1998.

[11] J. Qi and R. H. Huesman, "Lesion detection and quantitation of positron emission mammography," in *Proceedings of IEEE Nuclear Science Symposium and Medical Imaging Conference*, pp. M14–4, San Diego, CA, 2001.

[12] J. Qi and R. M. Leahy, "Resolution and noise properties of MAP reconstruction for fully 3D PET," *IEEE Transactions on Medical Imaging*, vol. 19, pp. 493–506, 2000.

[13] J. Qi and R. H. Huesman, "Image properties of list mode likelihood reconstruction for a rectangular positron emission mammograph with DOI measurements," *IEEE Transactions on Nuclear Science*, vol. 48, pp. 1343–1349, 2001.

[14] R. H. Huesman, G. J. Klein, W. W. Moses, J. Qi, B. W. Reutter, and P. R. G. Virador, "List mode maximum likelihood reconstruction applied to positron emission mammography with irregular sampling," *IEEE Transactions on Medical Imaging*, vol. 19, pp. 532–537, 2000.

[15] R. Pani, F. Scopinaro, R. Pellegrini, A. Soluri, I. Weinberg, and G. DeVincentis, "The role of Compton background and breast compression on cancer detection in scintimammography," *Anticancer Research*, vol. 17, pp. 1645–1649, 1997.